Effect of collagen fibril orientation on the anisotropic properties of peri-implant bone

Lucas Colabella, Salah Naili, Sophie Le Cann, Guillaume Haiat

Effect of collagen fibril orientation on the anisotropic properties of peri-implant bone

Lucas Colabella[1,2], Salah Naili[3], Sophie Le Cann[1] and Guillaume Haiat[1*]

[1]CNRS, Univ Paris Est Creteil, Univ Gustave Eiffel, UMR 8208, MSME, F-94010, Creteil, France.
[2]INTEMA, CONICET, Av. Cristóbal Colón 10850, Mar del Plata, B7606BWV, Argentina.
[3]Univ Paris Est Creteil, Univ Gustave Eiffel, CNRS, UMR 8208, MSME, F-94010, Creteil, France.

*Corresponding author(s). E-mail(s): haiat@u-pec.fr;
Contributing authors: lucas.colabella@u-pec.fr; naili@u-pec.fr; sophie.le-cann@cnrs.fr;

Abstract

In orthopedic and dental surgery, the implantation of biomaterials within the bone to restore the integrity of the treated organ has become a standard procedure. Their long-term stability relies on the osseointegration phenomena, where bone grows onto and around metallic implants, creating a bone-implant interface. Bone is a highly hierarchical material that evolves spatially and temporally during this healing phase. A deeper understanding of its biomechanical characteristics is needed, as they are determinants for surgical success. In this context, we propose a multiscale homogenization model to evaluate the effective elastic properties of bone as a function of the distance from the implant, based on the tissue's structure and composition at lower scales. The model considers three scales: hydroxyapatite foam (nanoscale), ultrastructure (microscale), and tissue (mesoscale). The elastic properties and the volume fraction of the elementary constituents of bone matrix (mineral, collagen, and water), the orientation of the collagen fibril relative to the implant surface, and the mesoscale porosity constitute the input data of the model. The effect of a spatiotemporal variation in the collagen fibrils' orientation on the bone anisotropic properties in the proximity of the implant was investigated. The findings revealed a strong variation of the components of the effective elasticity tensor of the bone as a function of the distance from the implant. The effective elasticity appears to be primarily sensitive to the porosity (mesoscale) rather than to the collagen fibrils' orientation (sub-micro scale). However, the orientation of the fibrils has a significant influence on the isotropy of the bone. When analyzing the symmetry properties of the effective elasticity tensor, the ratio between the isotropic and hexagonal components is determined by a combination of the porosity and the fibrils' orientation. A decrease in porosity leads to a decrease in bone isotropy and, in turn, an increase in the impact of the fibrils' orientation. These results demonstrate that the collagen fibril orientation should be taken into account to properly describe the effective elastic anisotropy of bone at the organ scale.

Keywords: bone, implant, multiscale, homogenization, collagen orientation

1 Introduction

Longer lifespans, stress, and poor nutritional practices are contributing factors to disorders that worsen bone quality and cause teeth loss (Fontaine and Barofsky, 2001). Moreover, active lifestyles and traffic and workplace accidents frequently lead to injuries (Kurtz et al, 2007). In orthopedic and dental surgery, the implantation of biomaterials inside the bone to restore the integrity of the treated organ has become a standard procedure. Implants and joint prostheses have significantly improved maxillofacial surgery (to restore missing teeth or support craniofacial reconstructions) and the treatment of joint degeneration (hip, knee, etc). A fast, robust, and long-lasting bond between the implant and the bone, *i.e.* adequate osseointegration, is the goal of current orthopedic and dental implant therapies (Gao et al, 2019).

The growth of bone around and onto the metallic foreign object leads to the formation of a bone-implant interface, which evolves as bone remodels (Albrektsson et al, 1981; Shah et al, 2019). An inability to obtain a bounded bone-implant contact is a common reason for early implant failure (during the first six months of implantation), which is one of the most common causes of failure in dental surgery (Chrcanovic et al, 2016; Grisar et al, 2017). It is difficult to determine the exact causes of osseointegration failure, which may result from a variety of implant-, surgery-, and patient-related variables (Amengual-Peñafiel et al, 2019; Albrektsson et al, 2017). A deeper understanding of the biomechanical characteristics of the bone-implant interface and the surrounding bone is needed to increase implant stability and decrease surgical failure risks (Haïat et al, 2014; Wirth et al, 2011).

Bone is a hierarchical anisotropic composite material that is strong and lightweight at the same time (Gao and Sevostianov, 2016). Mineralized bone (at the scale of 10-100 nm) is made of fundamental elements including water, collagen molecules, and hydroxyapatite crystals. The ultrastructure (at the scale of 1-10 µm), is constituted of mineralized collagen fibers embedded in a mineral foam. At the microscale, bone is organized either in a compact pattern (cortical bone) or a spongy pattern (cancellous bone). Cortical bone stiffness is given mainly by its porosity (Cai et al, 2019). However, bone ultrastructure orientation and arrangement are predictors of mechanical properties such as bone strength or elastic modulus (Georgiadis et al, 2016). Moreover, earlier studies have shown that peri-implant bone nanostructure is affected by the presence of ceramic and metallic implants (Hoerth et al, 2014a; Bünger et al, 2010; Le Cann et al, 2020). However, little is known about how those lower-scale changes impact the macroscale effective mechanical behavior of the bone-implant system.

A common approach to retrieve bone mechanical or acoustical properties consists in coupling 3-D reconstructions obtained from high-resolution imaging techniques with numerical simulation tools (Chevalier et al, 2007; Haïat et al, 2007, 2008). High-resolution Finite Element (FE) models are constructed from bone microstructures which are digitized using micro Computed Tomography (micro-CT) or *in vivo* high-resolution peripheral quantitative CT (HR-pQCT) scanners. FE analyses are used to compute bone effective elastic properties (Rietbergen et al, 1998, 1996; Ulrich et al, 1999; Pistoia et al, 2001), to predict bone strength (Rietbergen and Ito, 2015) and to conduct multiscale analyses (Podshivalov et al, 2011a,b). These models assume a linear elastic behavior of the material at the ultrastructure scale, whose mechanical properties are obtained via micro and nanoindentation tests Rodriguez-Florez et al (2014).

Another strategy to characterize the bone mechanical behavior consists in using its hierarchical organization together with empirical relations on its composition to build a multiscale homogenization model able to determine the elastic tensor at the scale of the organ (Hellmich et al, 2008; Sansalone et al, 2010, 2012; Gagliardi et al, 2018; Hellmich et al, 2022; Hamed and Jasiuk, 2012). In this way, bone stiffness can be obtained using only the information on the volume fraction of each constituent assuming a simplified structure at each scale considered. Several authors used this model to compute the elastic properties of trabecular (Hellmich et al, 2004b; Hamed et al, 2012) and cortical (Vaughan et al, 2012; Hamed et al, 2010; Martínez-Reina et al, 2011; Barkaoui et al, 2013) bone and to predict bone remodeling (Colloca et al, 2014). However, to the best of the authors' knowledge, it was never used to analyze the peri-implant bone. Furthermore, even if

classical computed tomography provides information on the microstructure, its spatial resolution is insufficient to get information on the geometrical arrangement of the ultrastructure. X-ray-based scattering techniques, such as small-angle X-ray scattering (SAXS), are sensitive to the crystal structure and periodic arrangement of bone minerals and can be used to retrieve information about mineral platelet orientation and thickness (Wagermaier et al, 2013; Turunen et al, 2016; Mathavan et al, 2018; Liu et al, 2010; Hoerth et al, 2014b) which can be linked to the collagen fibrils' orientation.

This paper aims to determine the spatial variation of the elastic tensor of the peri-implant bone during healing using a three-scale homogenization method that uses as input experimental data spatial variations of porosity and platelet orientation obtained from SAXS measurements of animal samples. Such an approach can be used to relate anatomical variations of porosity and platelet orientation to changes in peri-implant bone biomechanical properties.

2 Materials and methods

2.1 Multiscale homogenization model

A multiscale homogenization model was developed to compute the effective elastic properties of bone at the organ scale as a function of the distance from the implant. This model is based on the previous works of Haïat et al (2014) and Sansalone et al (2010). Three scales are considered: hydroxyapatite foam (HF), ultrastructure (US), and tissue (T) (see Fig. 1) which are respectively associated with three length scales (several hundred nanometers, several micrometers, and several hundred micrometers to several millimeters). The elastic properties and the volume fraction of the elementary constituents of the bone matrix (hydroxyapatite (HA), collagen (col), and water (W)), the orientation of the collagen fibrils relative to the implant surface (θ), and the bone porosity (ϕ_P) constitute the input data of the model. At each scale, the continuum micromechanics theory based on the Eshelby's representation of the uniform elastic field inside the ellipsoidal inclusion is applied (Suquet, 1997). Inclusions of different shapes (cylindrical or spherical) with different material properties (Laws, 1977a, 1985) are considered at each scale. In what follows, the position vector $\mathbf{x}$ is specified through the Cartesian coordinates (x_1, x_2, x_3) with respect to a Cartesian reference frame $\mathbf{R}(\mathrm{O};\ \mathbf{e}_1, \mathbf{e}_2, \mathbf{e}_3)$, where O is the origin of the space and $(\mathbf{e}_1, \mathbf{e}_2, \mathbf{e}_3)$ is an orthonormal basis of this space.

The homogenization methods based on continuum micromechanics can estimate the homogenized elasticity tensor of a representative volume element (RVE) comprised of several phases with different distributions and shapes, which can be organized in a matrix/inclusion-like microstructure or entirely disordered. The homogenized elasticity tensor turns out to be a weighted sum over the phases:

$$\mathbb{C}^{Hom} = \sum_r \phi_r \, \mathbb{C}^r : \mathbb{A}^r, \tag{1}$$

where ϕ_r, $\mathbb{C}^r$, and $\mathbb{A}^r$ are the volume fraction, the elastic tensor, and the localization tensor of the phase r, respectively. The symbol ":" in Eq. 1 denotes a double contraction of adjacent indexes of any couple of tensors. Note that the following condition is required: $\sum_r \phi_r = 1$. The fourth-order localization tensor links the microscopic infinitesimal strain field $\boldsymbol{\epsilon}(x)$ with the macroscopic infinitesimal strain $\mathbf{E}$, *i.e.* $\boldsymbol{\epsilon}(\mathbf{x}) = \mathbb{A}^r(\mathbf{x}) : \mathbf{E}$. It can be shown that the expression of $\mathbb{A}^r$ reads (see for instance Zaoui (2002)):

$$\mathbb{A}^r = \left(\mathbb{I} + \mathbb{P}^r : (\mathbb{C}^r - \mathbb{C}^0)\right)^{-1} : \left[\sum_s \phi_s \left(\mathbb{I} + \mathbb{P}^s : (\mathbb{C}^s - \mathbb{C}^0)\right)^{-1}\right]^{-1}, \tag{2}$$

where $\mathbb{P}^r$ is the fourth-order Hill tensor of the phase r embedded in the matrix phase, $\mathbb{C}^0$ is the elastic tensor of the reference material, $\mathbb{I}$ is the fourth-order identity tensor and s refers to the phase. The expression of the Hill tensor depends on the shape of the phase and on the elastic properties of the homogeneous host phase which is also called matrix phase.

The choice of the value of $\mathbb{C}^0$ leads to different estimates of the homogenized elasticity tensor $\mathbb{C}^{Hom}$. Two estimates are relevant in the context of this work (Nemat-Nasser and Hori, 2013): the Mori-Tanaka (MT) and the Self-Consistent (SC) estimates. The MT estimate is well suited

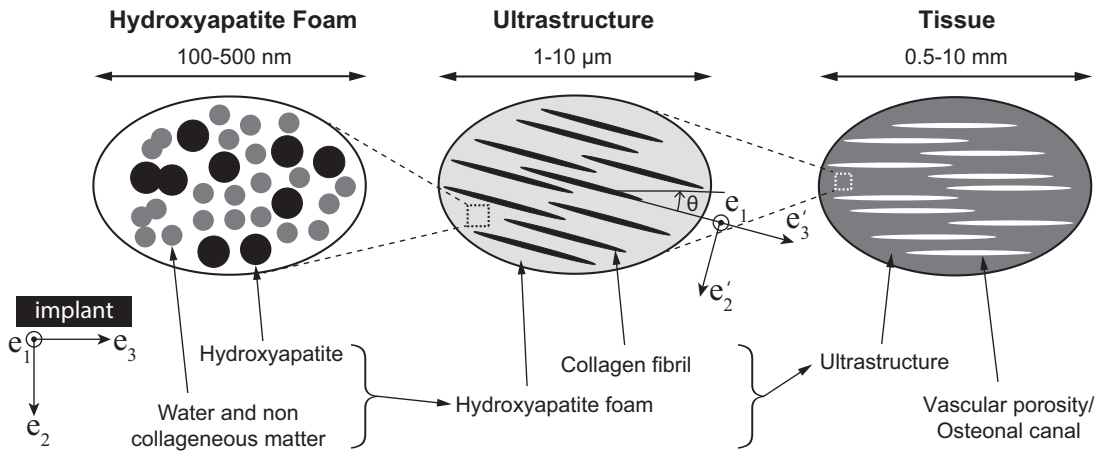

Scale	Phases (r, s)	Shape	$\mathbb{C}^{Hom}$	$\mathbb{C}^0$	Solution approach
Hydroxyapatite Foam (HF)	Hydroxyapatite (HA) Water (W)	Spherical Spherical	$\mathbb{C}^{HF}$	$\mathbb{C}^{HF}$	Self-consistent
Ultrastructure (US)	Hydroxyapatite Foam (HF) Collagen fibrils (col)	Matrix Cylindrical	$\mathbb{C}^{US}$	$\mathbb{C}^{HF}$	Mori-Tanaka
Tissue (T)	Ultrastructure (US) Pores (P)	Matrix Cylindrical	$\mathbb{C}^{T}$	$\mathbb{C}^{US}$	Mori-Tanaka

Fig. 1: Schematic description of the multiscale homogenization model with three length scales (several hundred nanometers, several micrometers, and several hundred micrometers to several millimeters). Material properties of the hydroxyapatite foam (left) and the ultrastructure (middle) are homogenized within each region of interest. In the tissue scale (right), the white regions schematically represent Haversian's canal or different vascular pores of the bone. The table at the bottom shows for each scale the phases that constitute it, the homogenized elastic tensor $\mathbb{C}^{Hom}$, the elastic tensor of the reference material $\mathbb{C}^0$, and the estimate used.

when the material microstructure is made up of uniformly dispersed inclusions in a homogeneous matrix. In this case, the effective matrix is an actual, well-identified phase and therefore $\mathbb{C}^0 = \mathbb{C}^{matrix}$. Then, the MT estimate of $\mathbb{C}^{Hom}$ can be readily computed from Eq. (1). The SC estimate is well suited when no actual matrix can be identified but the microstructure is rather made of interpenetrating (continuous or discontinuous) phases. In this case, the effective matrix is assumed to be the homogenized material itself and therefore $\mathbb{C}^0 = \mathbb{C}^{Hom}$. It follows that the SC estimate of $\mathbb{C}^{Hom}$ leads to an implicit equation (see Eq. (1)) which is solved iteratively using a fixed-point method.

In what follows, the equations to compute the effective elastic properties at each scale are described.

2.1.1 Hydroxyapatite foam

The hydroxyapatite foam can be seen as constituted by spherical inclusions of hydroxyapatite, water, and non-collageneous matter filling the entire space. This disordered structure motivates the use of an SC estimate to compute the homogenized elastic properties of the hydroxyapatite foam. Therefore, the elastic tensor is defined from Eq. (1) and Eq. (2) with $r, s \in [HA, W]$ as:

$$\mathbb{C}^{HF} = \left[\phi_{HA}\,\mathbb{C}^{HA} : \left(\mathbb{I} + \mathbb{P}^{HA} : (\mathbb{C}^{HA} - \mathbb{C}^{HF})\right)^{-1} + \phi_W\,\mathbb{C}^{W} : \left(\mathbb{I} + \mathbb{P}^{W} : (\mathbb{C}^{W} - \mathbb{C}^{HF})\right)^{-1}\right] : \left[\phi_{HA}\left(\mathbb{I} + \mathbb{P}^{HA} : (\mathbb{C}^{HA} - \mathbb{C}^{HF})\right)^{-1} +$$

$$\phi_W \left(\mathbb{I} + \mathbb{P}^W : (\mathbb{C}^W - \mathbb{C}^{HF})\right)^{-1}]^{-1}, \quad (3)$$

The non-zero components of the Hill tensor $\mathbb{P}^r$ for spherical inclusions embedded in the isotropic host phase $\mathbb{C}^{MF}$ can be expressed in Voigt notation as (Parnell, 2016):

$$\begin{aligned}
P^r_{11} = P^r_{22} = &P^r_{33} = P^r_{1111} = \\
&\frac{2C^{HF}_{12} + 7C^{HF}_{44}}{15C^{HF}_{44}(C^{HF}_{12} + 2C^{HF}_{44})}, \\
P^r_{12} = P^r_{13} = &P^r_{23} = P^r_{1122} = \\
&- \frac{C^{HF}_{12} + C^{HF}_{44}}{15C^{HF}_{44}(C^{HF}_{12} + 2C^{HF}_{44})}, \\
P^r_{44} = P^r_{55} = &P^r_{66} = 4P^r_{2323} = \\
&\frac{2(3C^{HF}_{12} + 8C^{HF}_{44})}{15C^{HF}_{44}(C^{HF}_{12} + 2C^{HF}_{44})}.
\end{aligned} \quad (4)$$

The obtained elastic tensor for this mixture is isotropic.

2.1.2 Ultrastructure

At the scale of several micrometers, the matrix phase is the hydroxyapatite foam described in the first step and the collagen fibrils are modeled as cylindrical inclusions, which motivates the use of the MT estimate. To account for the observed variation of the orientation of the collagen fibrils (see Section 2.3.3), a rotation around the common $\mathbf{e}_1$-axis is introduced, resulting in the $\mathbf{e}'_3$-axis forming an angle θ with the $\mathbf{e}_3$-axis (see Fig. 1). The elastic tensor of the ultrastructure $\mathbb{C}^{US'}$ referred to a local orthonormal basis defined by $(\mathbf{e}'_1, \mathbf{e}'_2, \mathbf{e}'_3)$ is computed from Eq. (1) and Eq. (2) with $r, s \in [HF, col]$ as (Parnell, 2016):

$$\begin{aligned}
&\mathbb{C}^{US'} = \\
&\Big[\phi_{HF}\,\mathbb{C}^{HF} + \phi_{col}\,\mathbb{C}^{col} : \\
&\quad \left(\mathbb{I} + \mathbb{P}^{col} : (\mathbb{C}^{col} - \mathbb{C}^{HF})\right)^{-1}\Big] : \\
&\Big[\phi_{HF}\,\mathbb{I} + \phi_{col}\,\left(\mathbb{I} + \mathbb{P}^{col} : (\mathbb{C}^{col} - \mathbb{C}^{HF})\right)^{-1}\Big]^{-1}.
\end{aligned} \quad (5)$$

The non-zero components of the Hill tensor for cylindrical inclusions in an isotropic host phase can be expressed in Voigt notation as:

$$\begin{aligned}
P^{col}_{11} &= P^{col}_{22} = P^{col}_{1111} = \frac{1}{8}\frac{C^{HF}_{11} + 3C^{HF}_{44}}{C^{HF}_{11}C^{HF}_{44}} \\
P^{col}_{12} &= P^{col}_{1122} = \frac{1}{8}\frac{C^{HF}_{44} - C^{HF}_{11}}{C^{HF}_{11}C^{HF}_{44}} \\
P^{col}_{44} &= P^{col}_{55} = 4P^{col}_{2323} = \frac{1}{2C^{HF}_{44}} \\
P^{col}_{66} &= \frac{P^{col}_{11} - P^{col}_{12}}{2} = 4P^{col}_{1212} = \frac{1}{2}\frac{C^{HF}_{11} + C^{HF}_{44}}{C^{HF}_{11}C^{HF}_{44}}
\end{aligned} \quad (6)$$

The obtained elastic tensor for the ultrastructure is transversely isotropic with its plane of isotropy the $(\mathbf{e}'_1, \mathbf{e}'_2)$-plane (see Fig. 1). Thus, a change of basis is needed to express the elastic tensor $\mathbb{C}^{US}$ in the reference basis $(\mathbf{e}_1, \mathbf{e}_2, \mathbf{e}_3)$. This tensor is defined by:

$$C^{US}_{ijkl} = U_{im}\,U_{jn}\,U_{kp}\,U_{lq}\,C^{US'}_{mnpq}, \quad (7)$$

where U_{ij} (for $i, j = 1, ..., 3$) are the components of the transformation matrix $\mathbf{U}$ for a rotation around the $\mathbf{e}_1$-axis which are defined by:

$$\mathbf{U} = \begin{pmatrix} 1 & 0 & 0 \\ 0 & \cos\theta & -\sin\theta \\ 0 & \sin\theta & \cos\theta \end{pmatrix}. \quad (8)$$

In the relation (7), Einstein's summation convention is used, that is, repeated subscripts are implicitly summed over. Moreover, it should be noticed that while $\mathbb{C}^{US'}$ is transversely isotropic, $\mathbb{C}^{US}$ is anisotropic.

2.1.3 Tissue

At the organ scale, bone tissue is considered as composed of cylindrical pores embedded in the homogeneous continuous ultrastructure described in the previous scale. We assumed that the orientation of the vascular porosity is parallel to the implant surface, which is due to the design of the animal model described in Section 2.3.3. Under these conditions, the effective elastic tensor $\mathbb{C}^T$ of the bone is, as in the previous scales, computed from Eq. (1) and Eq. (2) with $r, s \in [US, W, P]$ as:

$$\mathbb{C}^T = \left[\phi_{US}\mathbb{C}^{US} + \phi_{WP}\mathbb{C}^W : \left(\mathbb{I} + \mathbb{P}^P : (\mathbb{C}^W - \mathbb{C}^{US})\right)^{-1}\right] : \left[\phi_{US}\mathbb{I} + \phi_W \left(\mathbb{I} + \mathbb{P}^P : (\mathbb{C}^W - \mathbb{C}^{US})\right)^{-1}\right]^{-1}, \quad (9)$$

where ϕ_{WP} is the volume fraction of the mesoscopic pores (or porosity), which are considered filled with water.

As described in the previous section, the elastic properties $\mathbb{C}^{US}$ of the homogeneous host phase are anisotropic. Therefore, the Hill tensor has no closed-form expression for any inclusion shape. So, for a cylindrical inclusion, the components of the Hill's tensor can be expressed in the integral form (Laws, 1977b):

$$P^P_{ijkl} = \frac{1}{8}\left[M_{ijkl} + M_{jikl} + M_{ijlk} + M_{jilk}\right], \quad (10)$$

where the components of the fourth-order tensor $\mathbb{M}$ are given by:

$$\mathbb{M}_{ijkl} = \frac{1}{\pi}\int_0^{2\pi} \frac{\xi_i K^{-1}_{jk} \xi_l}{\xi_1^2 + \xi_2^2}\, d\psi, \quad (11)$$

where $\boldsymbol{\xi} = \cos\psi\, \mathbf{e}_1 + \sin\psi\, \mathbf{e}_2$ is a unit vector of plane centered at the origin, and $\mathbb{K} = \boldsymbol{\xi} \cdot \mathbb{C}^{US}$. $\boldsymbol{\xi}$ is the acoustic tensor which can be written as follows:

$$\mathbf{K} = \cos^2\psi\, \mathbf{Q} + \cos\psi\, \sin\psi\, (\mathbf{R} + \mathbf{R}^T) + \sin^2\psi\, \mathbf{T}, \quad (12)$$

where the superscript T designates the transpose operator. The components of the 3×3-matrices $\mathbf{Q}, \mathbf{R}$ and $\mathbf{T}$ are defined by the following relations:

$$\begin{aligned} Q_{ik} &= C^{US}_{i1k1}, \\ R_{ik} &= C^{US}_{i1k2}, \quad \text{for } i,k = 1,...,3. \\ T_{ik} &= C^{US}_{i2k2}, \end{aligned} \quad (13)$$

The obtained elastic tensor for the bone $\mathbb{C}^T$ is anisotropic. It should be noticed that when the collagen fibers are oriented with their principal axis coincident with the principal axis of the pores, *i.e.* $\theta = 0$, $\mathbb{C}^T$ has transversely isotropic symmetry.

2.2 Elastic tensor decomposition

To study the anisotropic nature of bone at the organ scale, it is useful to decompose its elastic tensor into a sum of orthogonal tensors belonging to the different symmetry classes. Hence, elastic symmetries of the effective elastic tensor $\mathbb{C}^T$ of the bone were computed using the Matlab Seismic Anisotropy Toolkit (MSAT) by Walker and Wookey (2012). This is an implementation of the method by Browaeys and Chevrot (2004), who considered the elasticity tensor $\mathbb{C}$ as an elastic vector $\mathbf{X}$ with 21 orthogonal components:

$$\begin{aligned} \mathbf{X} = (&C_{11}, C_{22}, C_{33}, \sqrt{2}C_{23}, \sqrt{2}C_{13}, \sqrt{2}C_{12}, \\ &2C_{44}, 2C_{55}, 2C_{66}, 2C_{14}, 2C_{25}, 2C_{36}, \\ &2C_{34}, 2C_{15}, 2C_{26}, 2C_{24}, 2C_{35}, 2C_{16}, \\ &2\sqrt{2}C_{56}, 2\sqrt{2}C_{46}, 2\sqrt{2}C_{45}). \end{aligned} \quad (14)$$

Then, $\mathbf{X}$ is decomposed by a cascade of projections into a sum of vectors belonging to the symmetry classes triclinic, monoclinic, orthorhombic, tetragonal, hexagonal, and isotropic,

$$\mathbf{X} = \mathbf{X}_{tri} + \mathbf{X}_{mon} + \mathbf{X}_{ort} + \mathbf{X}_{tet} + \mathbf{X}_{hex} + \mathbf{X}_{iso}. \quad (15)$$

Finally, the symmetry class fractions are computed as

$$c_c = \|\mathbf{X}_c\|/\|\mathbb{C}\|, \quad (16)$$

where $c \in [iso, hex, tet, ort, mon, tri]$.

2.3 Experimental input

The model developed in Section 2.1 requires as input data the individual constituents' elastic properties, the description of the phase of each constituent in each RVE (composition of the tissue), the orientation of the collagen fibrils at the ultrastructure scale and the average porosity of the bone at the tissue scale.

2.3.1 Elastic properties of the experimental constituents

The elastic properties of the elementary constituents (collagen, hydroxyapatite, and water) were taken from Hellmich et al (2004a) and are shown in Tab. 1. Both water and mineral are isotropic materials, while the collagen fibrils are transversely isotropic, the isotropy plane being orthogonal to the $\mathbf{e}_3$-axis of the fibril.

2.3.2 Estimation of the volume fraction of each component of bone tissue

Bone tissue is considered to be composed of hydroxyapatite, collagen, and water leading to:

$$\phi_{HA} + \phi_{col} + \phi_W = 1. \tag{17}$$

The estimation of ϕ_{HA} is done using:

$$\phi_{HA} = \frac{\text{TMD}}{\rho_{HA}} \tag{18}$$

where ρ_{HA} is the mass density of hydroxyapatite and TMD is the tissue mineral density. In this work, the mineralization is assumed to be constant and $TMD = 1$ (Gagliardi et al, 2018). The reader is referred to Sansalone et al (2010) for a detailed description of the influence of mineralization on bone mechanical properties. Volume fractions of hydroxyapatite, collagen and water are computed from an empirical relation obtained through measurements of volume fractions in demineralized bone by solving the nonlinear system (Broz et al, 1995):

$$\frac{\phi_{col}}{\phi_W} = \alpha + \beta \times e^{\gamma \times \phi_{HA}} \tag{19}$$

where $\alpha = 0.36, \beta = 0.084$ and $\gamma = 6.7$.

2.3.3 Mineralized collagen fibrils orientation

The collagen orientation in the bone tissue close to an implant surface varies during osseointegration. To model this variation, experimental data were extracted from a study formerly conducted by our group (Le Cann et al, 2020). The techniques and relevant results are briefly described hereafter, the reader is referred to the publication for more detailed information.

A standardized Ti6Al4V coin-shaped implant model with a dedicated bone chamber (diameter 5 mm, height 3 mm) had been osseointegrated in rabbit tibiae for 7 weeks ($n = 4$) and 13 weeks ($n = 4$) (see Fig. 2A). The newly-formed bone close to the implant surface was exposed (2D slices) and scanned using Scanning small-angle X-ray scattering (SAXS), with a micro-focused setup (around $4000 \times 250\ \mu m^2$ with a pixel size of 5 μm) (see Fig. 2B). From the 2D scattering patterns, the average predominant mineral plate orientation (direction of the crystallographic c-axis) was determined, which is commonly accepted to reflect the mineralized collagen fibril principal orientation, as minerals align and wrap around the fibrils (Reznikov et al, 2018). To extract the spatial variation of the collagen fibril orientation in relation to the implant distance, data were averaged within 20 regions of interest (ROIs) corresponding to 10 μm thick horizontal bands parallel to the implant surface (see Fig. 2B).

The experimental data depicts a spatial variation of the collagen fibril orientation (θ) with the distance to the implant surface (see Fig. 2C, D, dashed lines). Both at 7 weeks and 13 weeks of healing time, the angle between the fibrils and the implant surface is close to zero in the proximity of the implant ($10° < \theta < 25°$ in the first 80 μm), gradually increasing the further we move away. The variation in the collagen fibrils' orientation is higher at earlier stages of healing.

2.3.4 Bone tissue porosity

From the same experimental data set and similar ROIs (see Section 2.3.3), bone tissue porosity ϕ_{WP} was estimated from the Bone Area/Total Area ratio, *i.e.* the number of pixels corresponding to the bone tissue over the total number of pixels in the ROI (see Fig. 2C, D, solid lines). ϕ_{WP} is relatively stable at 7 weeks (averaged porosity within the chamber of 84%) and globally decreases with healing time (average of 65% at 13 weeks), depicting a strong drop in the very first 40 μm close to the implant surface. As reference data, a bone porosity value of 8% was identified as a healthy target value (human cortical bone, Gagliardi et al (2018)).

Phase	Elastic proprieties given in GPa					ϕ
	C_{11}	C_{33}	C_{12}	C_{13}	C_{44}	
Water	2.3	2.3	2.3	2.3	0	0.31
Hydroxyapatite	142.5	142.5	52.7	52.7	44.9	0.33
Collagen	11.7	17.9	5.1	7.1	3.3	0.36

Table 1: Elastic properties of the elementary constituents (Hellmich et al, 2004a). Water and mineral are isotropic materials, while the collagen fibril is a transversely isotropic material, the isotropy plane being orthogonal to the $\mathbf{e}_3$-axis of the fibril.

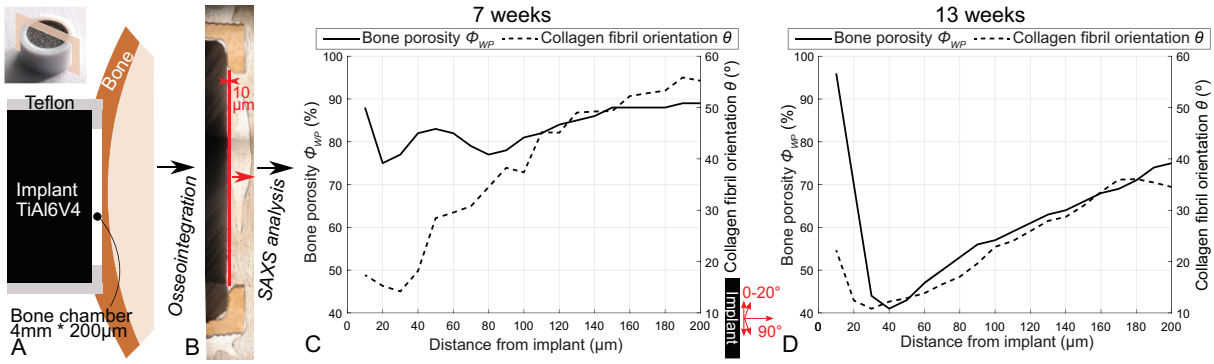

Fig. 2: Sectional scheme of the standardized implant model used in (Le Cann et al, 2020) (A). After osseointegration of 7 weeks and 13 weeks, specimens are explanted and analyzed with SAXS (B) to extract the spatial variation of bone porosity ϕ_{WP} (solid lines) and collagen fibril orientation θ (dashed lines) averaged in 10 μm thick bands parallel to the implant surface (C, D).

3 Results

3.1 Response of the model to variations in collagen fibril orientation and porosity

The evolution of the elastic tensor of the tissue $\mathbb{C}^T$ was computed as a function of the collagen fibrils orientation θ ($0° < \theta < 90°$) and for three different values of ϕ_{WP}: 8% (mature cortical bone), 65%, and 84% (bone during healing time) (see section 2.3.4) (Fig. 3). Additionally, Fig. 4 shows the evolution of $\mathbb{C}^T$ as a function of bone porosity ϕ_{WP} ($0 \leq \phi_{WP} \leq 100\%$) for different values of collagen fibrils orientation $\theta = 0°$, 45° and 90°.

When ϕ_{WP} increases, the values of each component of the elastic tensor of the bone $\mathbb{C}^T$ decrease (see Fig. 4), and, in particular, the value of C^T_{44} decreases faster than for the tensile elastic tensor components (*i.e.* C^T_{11}, C^T_{22}, and C^T_{33}), which is explained by the fact that the pores are filled with water, which has a lower stiffness compared to the ultrastructure and for which the shear components are equal to zero.

For a given porosity, C^T_{33} is maximum when $\theta = 0°$ *i.e.* when the principal axis of the collagen fibrils is aligned with the $\mathbf{e}_3$-axis. When the principal axis of the collagen fibrils is aligned with the $\mathbf{e}_2$-axis (*i.e.* for $\theta = 90°$), the behavior depends on the bone porosity. For low porosity, *i.e.* $\phi_{WP} = 0\%$ to 15%, $C^T_{22} > C^T_{33}$, while for higher porosities ($\phi_{WP} > 15\%$), $C^T_{22} < C^T_{33}$, which is in agreement with the behavior of the phases at the lower scale, *i.e.*, the ultrastructure. For a low value of ϕ_{WP}, *i.e.* a high content of ultrastructure, the anisotropic behavior is dominated by the collagen fibril orientation. Moreover, when $\phi_{WP} = 0\%$, *i.e.*, the only phase is the ultrastructure, C^T_{22} is higher than C^T_{33} for $\theta > 45°$, which indicates that the stiffness is conditioned by the collagen fibril orientation only. In contrast, when ϕ_{WP} is high, the effect of the orientation of the collagen fibrils

diminishes, which results in a low variation of the bone elastic tensor as a function of θ.

Regarding C_{44}^T (see Fig. 3), it is maximum when $\theta \sim 45°$ since at this point, the collagen fibrils are aligned with the principal stresses obtained with a pure shear load (Kaw, 2019).

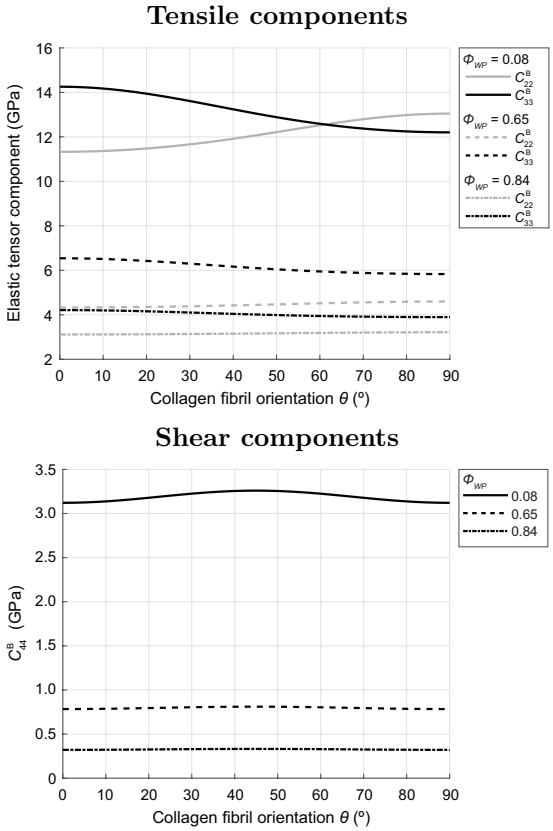

Fig. 3: Variation of the components of the elastic tensor of the tissue at the macro scale as a function of the collagen fibrils orientation θ for three different values of bone porosity ϕ_{WP}: 8% (mature cortical bone), 65%, and 84% (bone during healing time)

.

3.2 Analysis of the bone-implant interface

The variation of the elastic tensor of the tissue $\mathbb{C}^T$ was computed as a function of the distance from the implant based on experimental data (see Fig. 2C, D). Different scenarios were tested: the effect of a variation of i) bone porosity ϕ_{WP} alone, ii) collagen fibril orientation θ alone, and iii) ϕ_{WP} and θ combined (see Fig. 5). When analyzing the effect of a variation of ϕ_{WP} alone, the collagen fibrils were considered aligned with the pores ($\theta = 0$).

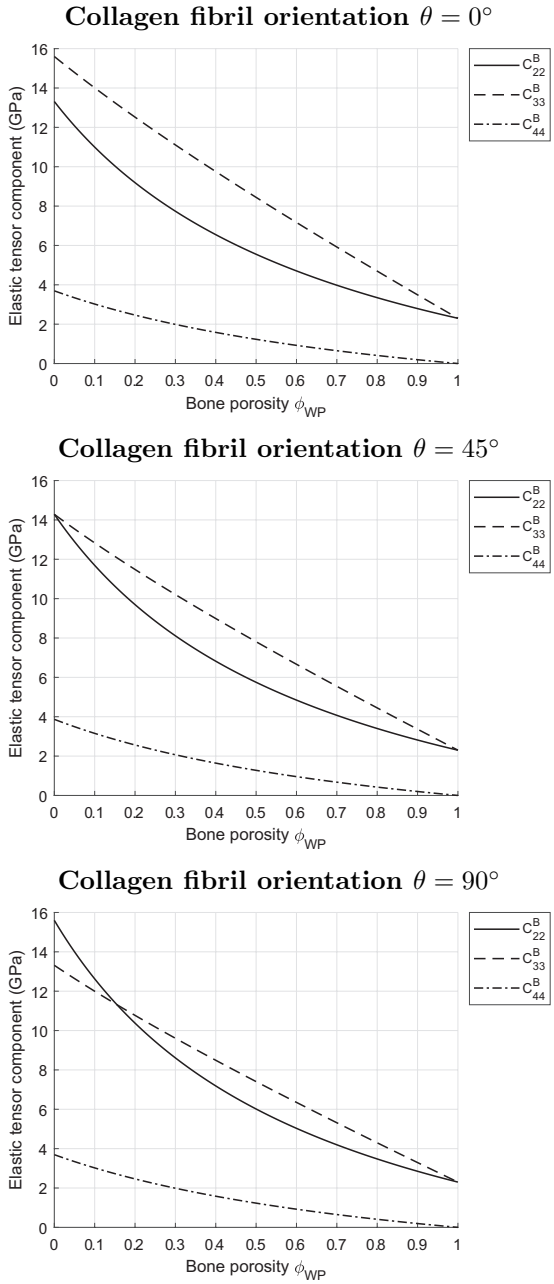

Fig. 4: Variation of the components of the elastic tensor of the tissue at the macro scale as a function of bone porosity ϕ_{WP} for three different values of the collagen fibril orientation θ: 0°, 45°, and 90°

When analyzing the effect of a variation of collagen fibril orientation alone, ϕ_{WP} was set as the average value in the bone chamber ($\phi_{WP} = 84\%$ for 7 weeks and $\phi_{WP} = 65\%$ for 13 weeks). Only components in the plane of the cross-section of the analyzed implants and for whom the collagen fibril orientation and ϕ_{WP} have a significant effect were considered (*i.e.* C_{22}^T, C_{33}^T and C_{44}^T).

The variation of the elastic tensor components as a function of the distance from the implant is similar when considering variations of ϕ_{WP} alone or when considering combined variations of ϕ_{WP} and θ (see Fig. 5). In both those cases, the spatial mechanical responses globally follow the spatial variation of the bone porosity (see Fig. 2). At 7 weeks of healing time, the maxima of all components are located at 20 μm from the implant, while the minima are in the ROI furthest from the implant (200 μm), towards mature bone. At 13 weeks, all minima have moved to the ROI closest to the implant, and all maxima are at 40 μm from the implant. There is no variation of the elastic tensor components when only θ varies, for a given ϕ_{WP}.

The tissue elastic tensor is shown to be mostly orthotropic with $0.1\% < c_{tri} < 1.1\%$ and $c_{mon} = 0$ (see decomposition in Fig. 6). At 7 weeks of healing time, the isotropic symmetry is almost constant, with a mean value of 91 % and a standard deviation of 2%. At 13 weeks, the isotropic symmetry shows a sharp decrease in the ROIs closest to the implant, going from 97% to 84% at 30 μm from the implant, and a nearly constant value after that region, with a mean value of 86% and a standard deviation of 3%.

4 Discussion

A deeper understanding of how the bone ultrastructure biomechanical properties change in the presence of an implant is essential to understand why and how an implant could later loosen and fail. This study constitutes one of the first attempts to analyze the effect of a variation in the collagen fibrils' orientation on the mechanical properties of the peri-implant bone using data obtained from a micro-focused SAXS setup and a bone chamber model. A multiscale homogenization model was applied, leading to the estimation of the homogenized anisotropic mechanical properties of the bone at the organ level. An originality of this approach is that it takes into account not only the shape of the collagen fibrils and the mesoscopic pores but also the relative orientation between them.

Collagen fibril orientation influence on bone mechanical behavior varies with the porosity

Considering the realistic bone tissue conditions studied within this work (*i.e.* bone porosity between 41% and 96% and collagen fibril orientation between 10° and 50°, see Fig. 2), the variation of all elastic tensor components is negligible when only the collagen fibril orientation changes (see Fig. 5), while outside these newly-formed bone experimental values, *e.g.* when considering mature cortical bone tissue with average porosity of ∼5-10% (Gagliardi et al, 2018), the elastic tensor components are affected by the collagen fibrils orientation (see Fig. 3). As the porosity decreases, the tissue content increases and the anisotropic behavior starts to be dominated by the collagen fibril orientation. Outside these conditions, the pores, filled with water, dominate the mechanical response.

The bone mechanical behavior evolves as a function of the distance from the implant

The elastic tensor undergoes strong spatial variation within the bone chamber, especially at the late healing time point when the bone is denser. Within the first 40 μm, the values of the elastic components are increased by 3 times, which can be explained by the substantial drop in local bone porosity observed experimentally within that region (see Fig. 2D, solid lines). Cai et al (2019) similarly concluded that porosity explains most of the variations of the non-zero stiffness constants in mature cortical bone (2 to 20% porosity). Even when after 13 weeks bone is not mature, it can be seen that the high porosity ϕ_{WP} variation has a strong impact on its mechanical response. At early time points, despite a larger spatial variation in collagen orientation (see Fig. 2C, dash-dotted lines), the high and stable porosity value (oscillating around 84%) explains the low variation of the tissue stiffness within the bone chamber. The estimation of bone porosity includes not only the porosity in the already formed bone (which has cylindrical shapes), but also the spaces within

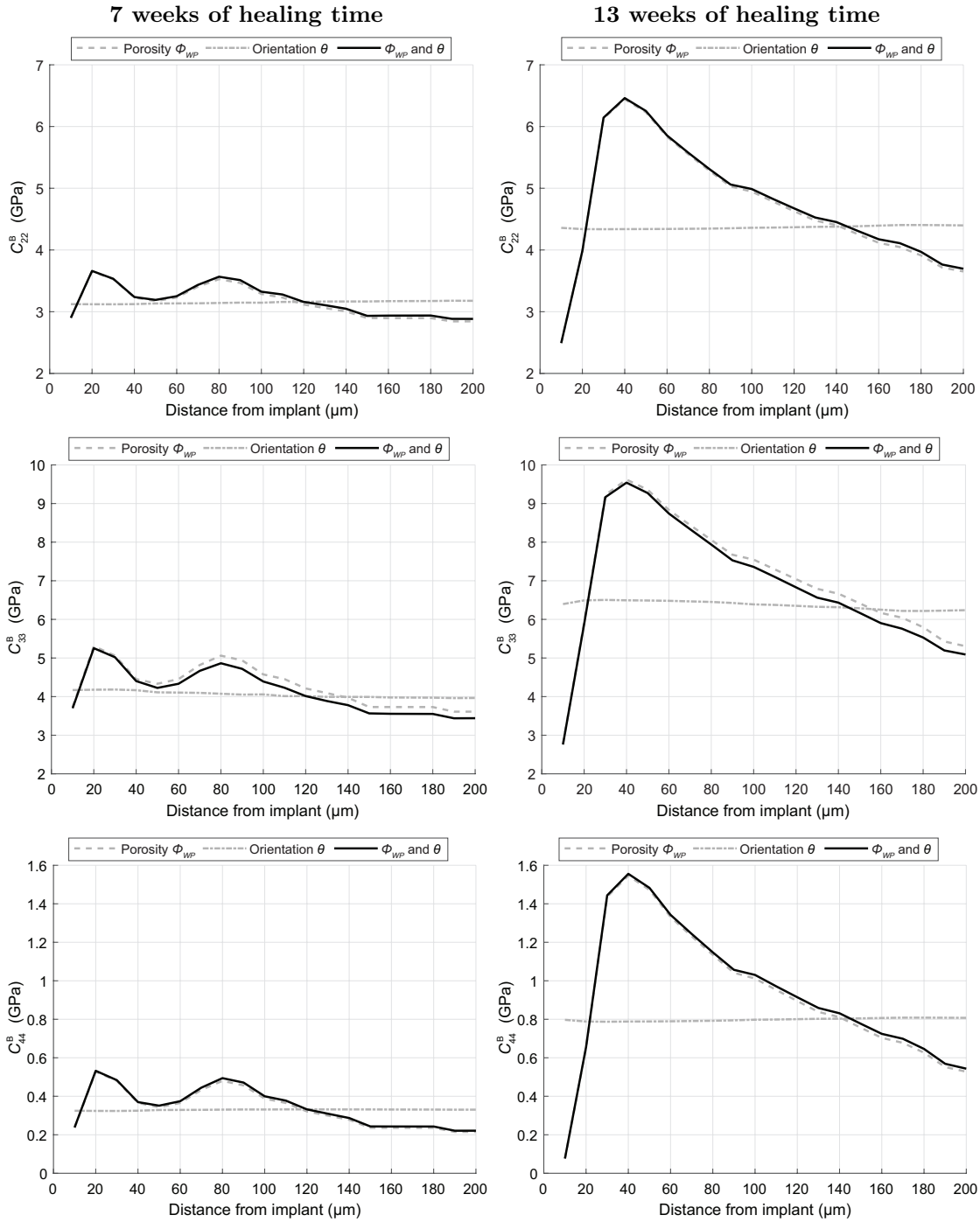

Fig. 5: Variation of the components of the elastic tensor of the tissue as a function of the distance from the implant at 7 weeks (left) and 14 weeks of healing time (right). ϕ_{WP} (dashed lines) corresponds to the response of the model to the variation of bone porosity alone, with $\theta = 0$. θ (dash-dotted lines) is the response to the variation of the collagen fibril orientation alone, for a fixed ϕ_{WP} ($\phi_{WP} = 84\%$ for 7 weeks and $\phi_{WP} = 65\%$ for 13 weeks). ϕ_{WP} and θ (solid lines) correspond to the combined variation of bone porosity and collagen fibril orientation.

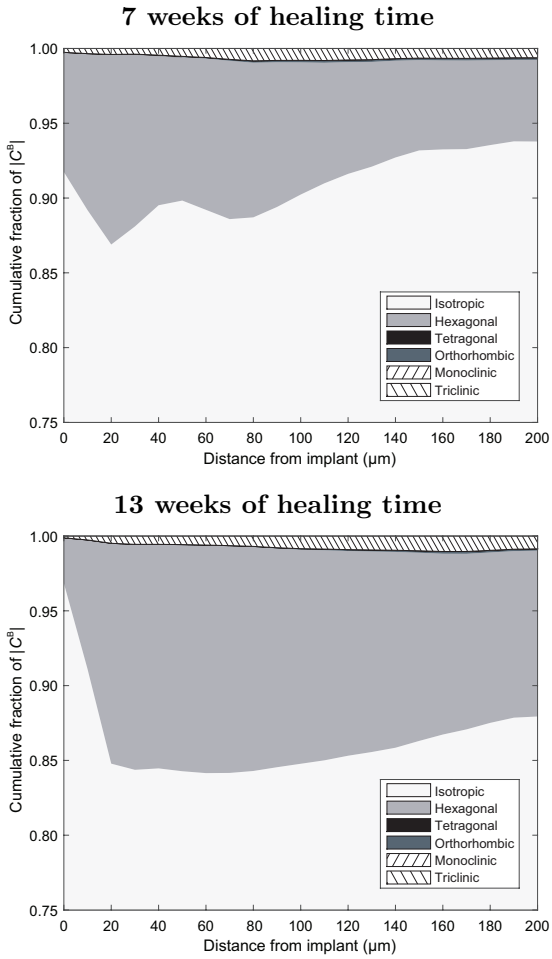

Fig. 6: Symmetry class decomposition of the elastic tensors as a function of the distance from the implant.

the bone chamber that the bone has not yet filled (bone is both formed and remodeled after introducing the implant). Thus, the high porosity observed at the close interface (first 40 μm) is likely to be caused not only by the bone porosity itself (cylindrical pores) but also by a low bone-implant contact ratio. This results in the mechanical response of the bone tissue at early healing times being mainly that of the pores (water-filled) and not that of the ultrastructure (composed of a mineral phase and collagen fibers). This limitation of the model is discussed in more detail below.

The nano- and micro-structural changes during healing have an impact on the mechanical behavior at higher scales

As healing proceeds, the reduction in ϕ_{WP} reflects both the formation of new bone and a decrease of porosity in the previously formed bone, as the tissue grows and densifies (Le Cann et al, 2020). At the nanoscale, the collagen fibrils tend to align better with the implant surface. Mechanically, the alignment of the collagen fibrils leads to a global increase in the elastic tensor component values in the reference frame $\mathbf{R}(\mathrm{O};\ \mathbf{e}_1, \mathbf{e}_2, \mathbf{e}_3)$. Moreover, the hexagonal symmetry of the elastic tensor increases with healing (see Fig. 6). An elastic medium with hexagonal symmetry is equivalent to a transversely isotropic medium (Browaeys and Chevrot, 2004). This equivalence suggests that at early healing stages, a combination of a higher porosity and a stronger misalignment between the collagen fibrils and the vascular porosity (see Fig. 2) results in the bone tissue being isotropic rather than orthotropic, which is the expected mechanical behavior in mature bone (Cowin, 2001).

Limitations

Limits on experimental data. This study is based on 2D experimental data from 8 bone-implant specimens (n = 4 per time point) which represent a limited dataset. However, this data still represents the largest and most refined SAXS study to investigate the spatial evolution of the bone ultrastructure at the bone-implant interface. Moreover, as only mineral crystals diffracting in the beam direction contributed to the average orientation measured here, the analysis is currently limited to the analyzed radial direction and needs to be extended to other cutting directions in the future, particularly along the longitudinal direction, where bone presents a higher degree of orientation (Törnquist et al, 2020).

Effect of bone mineralization Bone mineralization is not included in the analysis and would be needed to clarify the mechanical response close to the implant. It was not possible to measure the degree of mineralization of the samples used in this work, and a constant value was assumed for all samples and healing times. X-ray micro-tomography is frequently used to obtain the degree of tissue mineralization as the grey

levels obtained in the reconstructed images are linked to the local content of minerals. However, such a technique is difficult to conduct close to metallic implants due to frequent imaging artifacts (Barrett and Keat, 2004; Törnquist et al, 2021). Previous numerical work has shown an increase in bone tissue stiffness with the increase of the mineralization on cortical bone (Sansalone et al, 2010). Thus, since bone formation and remodeling close to implants leads to significant changes in the degree of mineralization (in particular reduction) (Allen and Burr, 2014) the assumption made in this work can lead to an overestimation of the tissue stiffness.

Limitation of the model. The porosity was modeled by cylindrical canals parallel to the implant surface. However, during bone healing, the pore shape may differ from Haversian canals and may be composed of large cavities filled with marrow. These cavities have irregular form and their mechanical effects might not be suitably described by cylindrical pores. As in the case of the degree of mineralization, accounting for the real shape of the pores requires a much more detailed morphological analysis using X-ray micro-tomography images that should be addressed in further studies.

5 Conclusions

A multiscale homogenization model was proposed to compute the effective elastic properties of newly-formed bone (macroscale) as a function of the distance from the implant, based on experimentally obtained tissue structure and composition at lower scales. This method can be used to replace the complex structure of the peri-implant bone for a continuum model to analyze the spatiotemporal evolution of bone during the healing time. In this work, the effects of the porosity and the collagen fibrils orientation variations on the bone anisotropic properties in the proximity of the implant were investigated.

The findings revealed a strong variation of the components of the effective elasticity tensor of the bone tissue as a function of the distance from the implant. The effective elasticity is primarily sensitive to the porosity (mesoscale) rather than to the collagen fibrils' orientation (submicroscale). However, the orientation of the fibrils has a significant influence on the symmetry properties of the effective elasticity tensor. A decrease in porosity leads to a decrease in bone isotropy and an increase in the impact of the fibrils' orientation.

These results demonstrate that the collagen fibril orientation affects the effective elastic properties of the bone throughout the remodeling process in the proximity of an implant. Collagen fibril orientation should be taken into account to properly describe the effective elastic anisotropy of bone tissue at the organ scale.

Acknowledgements

This work has been supported by the European Union's Horizon 2020 research and innovation programme under the Marie Sklodowska-Curie grant agreement no. 101027554. This project has received funding from the project OrthAncil (ANR-21-CE19-0035-03) and from the project OrthoMat (ANR-21-CE17-0004).

Declarations

Funding

No funding was received to assist with the preparation of this manuscript.

Competing interests

The authors declare no competing interests.

Conflict of Interest

On behalf of all authors, the corresponding author states that there is no conflict of interest.

Ethics approval

N/A

Availability of data and materials

The data that support the findings of this study are available from the corresponding author upon request.

References

Albrektsson T, Brånemark PI, Hansson HA, et al (1981) Osseointegrated

Titanium Implants: Requirements for Ensuring a Long-Lasting, Direct Bone-to-Implant Anchorage in Man. Acta Orthopaedica Scandinavica 52(2):155–170. https://doi.org/10.3109/17453678108991776

Albrektsson T, Chrcanovic B, Östman P, et al (2017) Initial and long-term crestal bone responses to modern dental implants. Periodontology 2000 73(1):41–50. https://doi.org/10.1111/prd.12176

Allen MR, Burr DB (2014) Chapter 4 - bone modeling and remodeling. In: Burr DB, Allen MR (eds) Basic and Applied Bone Biology. Academic Press, San Diego, p 75–90, https://doi.org/https://doi.org/10.1016/B978-0-12-416015-6.00004-6, URL https://www.sciencedirect.com/science/article/pii/B9780124160156000046

Amengual-Peñafiel L, Brañes-Aroca M, Marchesani-Carrasco F, et al (2019) Coupling between Osseointegration and Mechanotransduction to Maintain Foreign Body Equilibrium in the Long-Term: A Comprehensive Overview. Journal of Clinical Medicine 8(2):139. https://doi.org/10.3390/jcm8020139

Barkaoui A, Chamekh A, Merzouki T, et al (2013) Multiscale approach including microfibril scale to assess elastic constants of cortical bone based on neural network computation and homogenization method. International Journal for Numerical Methods in Biomedical Engineering 30(3):318–338. https://doi.org/10.1002/cnm.2604

Barrett JF, Keat N (2004) Artifacts in ct: Recognition and avoidance. RadioGraphics 24(6):1679–1691. https://doi.org/10.1148/rg.246045065, URL https://doi.org/10.1148/rg.246045065, pMID: 15537976, https://arxiv.org/abs/https://doi.org/10.1148/rg.246045065

Browaeys JT, Chevrot S (2004) Decomposition of the elastic tensor and geophysical applications. Geophysical Journal International 159(2):667–678. https://doi.org/10.1111/j.1365-246X.2004.02415.x, URL http://gji.oxfordjournals.org/cgi/doi/10.1111/j.1365-246X.2004.02415.x

Broz J, Simske S, Greenberg A (1995) Material and compositional properties of selectively demineralized cortical bone. Journal of Biomechanics 28(11):1357–1368. https://doi.org/https://doi.org/10.1016/0021-9290(94)00184-6ISTEX, URL https://www.sciencedirect.com/science/article/pii/0021929094001846

Bünger MH, Oxlund H, Hansen TK, et al (2010) Strontium and Bone Nanostructure in Normal and Ovariectomized Rats Investigated by Scanning Small-Angle X-Ray Scattering. Calcified Tissue International 86(4):294–306. https://doi.org/10.1007/s00223-010-9341-8

Cai X, Brenner R, Peralta L, et al (2019) Homogenization of cortical bone reveals that the organization and shape of pores marginally affect elasticity. Journal of the Royal Society Interface 16(151):20180,911. https://doi.org/10.1098/rsif.2018.0911

Chevalier Y, Pahr D, Allmer H, et al (2007) Validation of a voxel-based fe method for prediction of the uniaxial apparent modulus of human trabecular bone using macroscopic mechanical tests and nanoindentation. Journal of Biomechanics 40(15):3333–3340. https://doi.org/https://doi.org/10.1016/j.jbiomech.2007.05.004

Chrcanovic B, Kisch J, Albrektsson T, et al (2016) Factors Influencing Early Dental Implant Failures. Journal of Dental Research 95(9):995–1002. https://doi.org/10.1177/0022034516646098

Colloca M, Blanchard R, Hellmich C, et al (2014) A multiscale analytical approach for bone remodeling simulations: Linking scales from collagen to trabeculae. Bone 64:303–313. https://doi.org/https://doi.org/10.1016/j.bone.2014.03.050, URL https://www.sciencedirect.com/science/article/pii/S8756328214001240

Cowin SC (2001) Bone Mechanics Handbook, 2nd edn. CRC Press, https://doi.org/10.1201/b14263

Fontaine KR, Barofsky I (2001) Obesity and health-related quality of life. Obesity Reviews 2(3):173–182. https://doi.org/10.1046/j.1467-789x.2001.00032.x

Gagliardi D, Sansalone V, Desceliers C, et al (2018) Estimation of the effective bone-elasticity tensor based on μCT imaging by a stochastic model. A multi-method validation. European Journal of Mechanics, A/Solids 69(October 2017):147–167. https://doi.org/10.1016/j.euromechsol.2017.10.004, URL https://doi.org/10.1016/j.euromechsol.2017.10.004

Gao X, Sevostianov I (2016) Connection between elastic and electrical properties of cortical bone. Journal of Biomechanics 49(5):765–772. https://doi.org/https://doi.org/10.1016/j.jbiomech.2016.02.019

Gao X, Fraulob M, Haïat G (2019) Biomechanical behaviours of the bone-implant interface: a review. Journal of The Royal Society Interface 16(156):20190,259. https://doi.org/10.1098/rsif.2019.0259

Georgiadis M, Müller R, Schneider P (2016) Techniques to assess bone ultrastructure organization: orientation and arrangement of mineralized collagen fibrils. Journal of The Royal Society Interface 13(119):20160,088. https://doi.org/10.1098/rsif.2016.0088

Grisar K, Sinha D, Schoenaers J, et al (2017) Retrospective Analysis of Dental Implants Placed Between 2012 and 2014: Indications, Risk Factors, and Early Survival. The International Journal of Oral & Maxillofacial Implants 32(3):649–654. https://doi.org/10.11607/jomi.5332

Hamed E, Jasiuk I (2012) Elastic modeling of bone at nanostructural level. Materials Science and Engineering: R: Reports 73(3-4):27–49. https://doi.org/10.1016/j.mser.2012.04.001

Hamed E, Lee Y, Jasiuk I (2010) Multiscale modeling of elastic properties of cortical bone. Acta Mechanica 213(1-2):131–154. https://doi.org/10.1007/s00707-010-0326-5

Hamed E, Jasiuk I, Yoo A, et al (2012) Multiscale modelling of elastic moduli of trabecular bone. Journal of The Royal Society Interface 9(72):1654–1673. https://doi.org/10.1098/rsif.2011.0814

Haïat G, Padilla F, Peyrin F, et al (2007) Variation of ultrasonic parameters with microstructure and material properties of trabecular bone: A 3d model simulation. Journal of Bone and Mineral Research 22(5):665–674. https://doi.org/https://doi.org/10.1359/jbmr.070209

Haïat G, Padilla F, Peyrin F, et al (2008) Fast wave ultrasonic propagation in trabecular bone: Numerical study of the influence of porosity and structural anisotropy. Journal of the Acoustical Society of America 123(3):1694–1705. https://doi.org/10.1121/1.2832611

Haïat G, Wang HL, Brunski J (2014) Effects of Biomechanical Properties of the Bone–Implant Interface on Dental Implant Stability: From In Silico Approaches to the Patient's Mouth. Annual Review of Biomedical Engineering 16(1):187–213. https://doi.org/10.1146/annurev-bioeng-071813-104854

Hellmich C, Barthélémy JF, Dormieux L (2004a) Mineral-collagen interactions in elasticity of bone ultrastructure - A continuum micromechanics approach. European Journal of Mechanics, A/Solids 23(5):783–810. https://doi.org/10.1016/j.euromechsol.2004.05.004ISTEX

Hellmich C, Ulm FJ, Dormieux L (2004b) Can the diverse elastic properties of trabecular and cortical bone be attributed to only a few tissue-independent phase properties and their interactions? Biomechanics and Modeling in Mechanobiology 2(4):219–238. https://doi.org/10.1007/s10237-004-0040-0

Hellmich C, Kober C, Erdmann B (2008) Micromechanics-based conversion of ct data into anisotropic elasticity tensors, applied to fe simulations of a mandible. Annals of Biomedical Engineering 36(1):108 – 122. https://doi.org/10.1007/s10439-007-9393-8

Hellmich C, Ukaj N, Smeets B, et al (2022) Hierarchical biomechanics: Concepts, bone as

prominent example, and perspectives beyond. Applied Mechanics Reviews 74(3). https://doi.org/10.1115/1.4055032

Hoerth RM, Katunar MR, Sanchez AG, et al (2014a) A comparative study of zirconium and titanium implants in rat: osseointegration and bone material quality. Journal of Materials Science: Materials in Medicine 25(2):411–422. https://doi.org/10.1007/s10856-013-5074-3

Hoerth RM, Seidt BM, Shah M, et al (2014b) Mechanical and structural properties of bone in non-critical and critical healing in rat. Acta Biomaterialia 10(9):4009–4019. https://doi.org/10.1016/j.actbio.2014.06.003

Kaw AK (2019) Mechanics of Composite Materials. CRC Press, https://doi.org/10.1201/9781420058291

Kurtz SM, Ong KL, Schmier J, et al (2007) Future Clinical and Economic Impact of Revision Total Hip and Knee Arthroplasty. The Journal of Bone & Joint Surgery 89(suppl_3):144–151. https://doi.org/10.2106/jbjs.g.00587

Laws N (1977a) The determination of stress and strain concentrations at an ellipsoidal inclusion in an anisotropic material. Journal of Elasticity 7(1):91–97. https://doi.org/10.1007/BF00041133

Laws N (1977b) A note on interaction energies associated with cracks in anisotropic solids. Philosophical Magazine 36(2):367–372. https://doi.org/dx.doi.org/10.1080/14786437708244940

Laws N (1985) A note on penny-shaped cracks in transversely isotropic materials. Mechanics of Materials 4(2):209–212. https://doi.org/10.1016/0167-6636(85)90017-1

Le Cann S, Törnquist E, Barreto IS, et al (2020) Spatio-temporal evolution of hydroxyapatite crystal thickness at the bone-implant interface. Acta Biomaterialia 116:391–399. https://doi.org/10.1016/j.actbio.2020.09.021

Liu Y, Manjubala I, Schell H, et al (2010) Size and habit of mineral particles in bone and mineralized callus during bone healing in sheep. Journal of Bone and Mineral Research 25(9):2029–2038. https://doi.org/10.1002/jbmr.84

Martínez-Reina J, Domínguez J, García-Aznar JM (2011) Effect of porosity and mineral content on the elastic constants of cortical bone: a multiscale approach. Biomechanics and Modeling in Mechanobiology 10(3):309–322. https://doi.org/10.1007/s10237-010-0236-4

Mathavan N, Turunen MJ, Guizar-Sicairos M, et al (2018) The compositional and nano-structural basis of fracture healing in healthy and osteoporotic bone. Scientific Reports 8(1):1591. https://doi.org/10.1038/s41598-018-19296-z

Nemat-Nasser S, Hori M (2013) Micromechanics: overall properties of heterogeneous materials. Elsevier

Parnell WJ (2016) The Eshelby, Hill, Moment and Concentration Tensors for Ellipsoidal Inhomogeneities in the Newtonian Potential Problem and Linear Elastostatics. Journal of Elasticity 125(2):231–294. https://doi.org/10.1007/s10659-016-9573-6, URL http://dx.doi.org/10.1007/s10659-016-9573-6

Pistoia W, Rietbergen Bv, Laib A, et al (2001) High-Resolution Three-Dimensional-pQCT Images Can Be an Adequate Basis for In-Vivo μFE Analysis of Bone. Journal of Biomechanical Engineering 123(2):176–183. https://doi.org/10.1115/1.1352734

Podshivalov L, Fischer A, Bar-Yoseph P (2011a) 3D hierarchical geometric modeling and multiscale FE analysis as a base for individualized medical diagnosis of bone structure. Bone 48(4):693–703. https://doi.org/10.1016/j.bone.2010.12.022

Podshivalov L, Fischer A, Bar-Yoseph P (2011b) Multiscale FE method for analysis of bone micro-structures. Journal of the Mechanical Behavior of Biomedical Materials 4(6):888–899. https://doi.org/10.1016/j.jmbbm.2011.03.003

Reznikov N, Bilton M, Lari L, et al (2018) Fractal-like hierarchical organization of bone begins at the nanoscale. Science 360(6388):eaao2189. https://doi.org/10.1126/science.aao2189, URL https://www.science.org/doi/abs/10.1126/science.aao2189, https://arxiv.org/abs/https://www.science.org/doi/pdf/10.1126/science.aao2189

Rietbergen Bv, Ito K (2015) A survey of micro-finite element analysis for clinical assessment of bone strength: The first decade. Journal of Biomechanics 48(5):832–841. https://doi.org/10.1016/j.jbiomech.2014.12.024

Rietbergen BV, Odgaard A, Kabel J, et al (1996) Direct mechanics assessment of elastic symmetries and properties of trabecular bone architecture. Journal of Biomechanics 29(12):1653–1657. https://doi.org/10.1016/s0021-9290(96)80021-2

Rietbergen BV, Odgaard A, Kabel J, et al (1998) Relationships between bone morphology and bone elastic properties can be accurately quantified using high-resolution computer reconstructions. Journal of Orthopaedic Research 16(1):23–28. https://doi.org/10.1002/jor.1100160105

Rodriguez-Florez N, Oyen ML, Shefelbine SJ (2014) Age-related changes in mouse bone permeability. Journal of Biomechanics 47(5):1110–1116. https://doi.org/10.1016/j.jbiomech.2013.12.020

Sansalone V, Naili S, Bousson V, et al (2010) Determination of the heterogeneous anisotropic elastic properties of human femoral bone: From nanoscopic to organ scale. Journal of Biomechanics 43(10):1857–1863. https://doi.org/10.1016/j.jbiomech.2010.03.034

Sansalone V, Bousson V, Naili S, et al (2012) Anatomical distribution of the degree of mineralization of bone tissue in human femoral neck: Impact on biomechanical properties. Bone 50(4):876–884. https://doi.org/10.1016/j.bone.2011.12.020

Shah FA, Thomsen P, Palmquist A (2019) Osseointegration and current interpretations of the bone-implant interface. Acta Biomaterialia 84:1–15. https://doi.org/10.1016/j.actbio.2018.11.018

Suquet P (1997) Continuum Micromechanics. Springer, Vienna, https://doi.org/10.1007/978-3-7091-2662-2

Turunen MJ, Kaspersen JD, Olsson U, et al (2016) Bone mineral crystal size and organization vary across mature rat bone cortex. Journal of Structural Biology 195(3):337–344. https://doi.org/https://doi.org/10.1016/j.jsb.2016.07.005, URL https://www.sciencedirect.com/science/article/pii/S1047847716301460

Törnquist E, Isaksson H, Turunen MJ (2020) Mineralization of cortical bone during maturation and growth in rabbits. Journal of Bone and Mineral Metabolism 38(3):289–298. https://doi.org/10.1007/s00774-019-01068-y

Törnquist E, Cann SL, Tudisco E, et al (2021) Dual modality neutron and x-ray tomography for enhanced image analysis of the bone-metal interface. Physics in Medicine and Biology 66(13):135,016. https://doi.org/10.1088/1361-6560/ac02d4, URL https://dx.doi.org/10.1088/1361-6560/ac02d4

Ulrich D, Rietbergen Bv, Laib A, et al (1999) The ability of three-dimensional structural indices to reflect mechanical aspects of trabecular bone. Bone 25(1):55–60. https://doi.org/10.1016/s8756-3282(99)00098-8

Vaughan T, McCarthy C, McNamara L (2012) A three-scale finite element investigation into the effects of tissue mineralisation and lamellar organisation in human cortical and trabecular bone. Journal of the Mechanical Behavior of Biomedical Materials 12:50–62. https://doi.org/https://doi.org/10.1016/j.jmbbm.2012.03.003, URL https://www.sciencedirect.com/science/article/pii/S1751616112000835

Wagermaier W, Gourrier A, Aichmayer B (2013) Materials Design Inspired by Nature : Function Through Inner Architecture. Smart Materials Series pp 46–73. https://doi.org/10.1039/

9781849737555-00046

Walker AM, Wookey J (2012) MSAT-A new toolkit for the analysis of elastic and seismic anisotropy. Computers and Geosciences 49:81–90. https://doi.org/10.1016/j.cageo.2012.05.031, URL http://dx.doi.org/10.1016/j.cageo.2012.05.031

Wirth AJ, Goldhahn J, Flaig C, et al (2011) Implant stability is affected by local bone microstructural quality. Bone 49(3):473–478. https://doi.org/10.1016/j.bone.2011.05.001ISTEX

Zaoui A (2002) Continuum micromechanics: Survey. J Eng Mech 128(8):808–816. https://doi.org/10.1061/(ASCE)0733-9399(2002)128:8(808)